Journal of Inorganic Biochemistry 194 (2019) 85–96

Contents lists available at ScienceDirect

Journal of Inorganic Biochemistry

journal homepage: www.elsevier.com/locate/jinorgbio

Palladium(II) complexes with salicylaldehyde ligands: Synthesis, characterization, structure, *in vitro* and *in silico* study of the interaction with calf-thymus DNA and albumins

Ariadni Zianna[a,*], George D. Geromichalos[a], Antonios G. Hatzidimitriou[a], Evdoxia Coutouli-Argyropoulou[b], Maria Lalia-Kantouri[a], George Psomas[a,*]

[a] Laboratory of Inorganic Chemistry, Department of Chemistry, Aristotle University of Thessaloniki, Thessaloniki GR-54124, Greece
[b] Laboratory of Organic Chemistry, Department of Chemistry, Aristotle University of Thessaloniki, Thessaloniki GR-54124, Greece

ARTICLE INFO

Keywords:
Palladium(II) complexes
Salicylaldehydes
Interaction with CT DNA
Interaction with serum albumins
in silico molecular docking

ABSTRACT

The synthesis and characterization of four palladium(II) complexes with substituted salicylaldehydes (X-saloH) having the general formula $[Pd(X\text{-}salo)_2]$ was undertaken. The complexes are formulated as $[Pd(3\text{-}OCH_3\text{-}salo)_2]$ **1**, $[Pd(5\text{-}NO_2\text{-}salo)_2]$ **2**, $[Pd(5\text{-}Cl\text{-}salo)_2]$ **3**, and $[Pd(5\text{-}Br\text{-}salo)_2]$ **4**. The structure of complex **1** was verified by single-crystal X-ray crystallography. Spectroscopic (UV–vis), and physicochemical (viscosity measurements) techniques were employed in order to study the binding of the complexes with calf-thymus (CT) DNA, while ethidium bromide (EB) displacement studies, performed by fluorescence emission spectroscopy, revealed the ability of the complexes to displace the DNA-bound EB. Intercalation is the most possible mode of interaction of the complexes with CT DNA. The interaction of the complexes with bovine (BSA) and human (HSA) serum albumin proteins was studied by fluorescence emission spectroscopy and the relatively high binding constants revealed the reversible binding of the complexes to the albumins. Molecular docking simulations on the crystal structure of HSA, BSA and CT DNA were employed in order to study *in silico* the ability of the studied complexes **1–4** to bind to these target macromolecules.

1. Introduction

The study of structure and properties of coordination compounds is a very large field of Inorganic Chemistry. The coordination of biologically active ligands to a metal ion may enhance or change the biological properties of the ligand, leading thus to the formation of novel compounds with improved characteristics. Palladium complexes are among the most-studied complexes along with Pt, Cu, Au and Ru [1]. Researchers' increasing interest to palladium complexes is mainly due to the fact that Pd compounds might be used as an alternative to *cisplatin* and other platinum complexes in cancer treatment [2]. Although the coordination modes of Pd(II) and Pt(II) are similar, their coordination compounds present different behavior, mainly because Pd complexes have a fast ligands-exchange capacity, almost 10^5 times higher than Pt (II) complexes, and are highly hydrolyzed [3]. Most of the reported palladium complexes have been studied for their anticancer [1] and antineoplasmatic activity [2]. Moreover, Pd complexes have been reported to exhibit *in vitro* antiviral, anti-fungal, antimicrobial [4], anti-inflammatory [5], and antioxidant properties [6]. The ligands used in these complexes are mainly N-, S- or P-donors [3]. The Pd coordination compounds with oxygen-donor ligands are less studied, despite the fact that carboxylates (O,O′-coordination mode) or dicarboxylates have been used in biologically active platinum compounds (oxaliplatin and carboplatin) because they are considered to increase water solubility and/or lipophilicity of the complexes. The formed chelate ring due to the coordination of two oxygens of the dicarboxylates increases the stability of the complexes and reduces the side-effects of platinum complexes [2].

Salicylaldehyde (saloH) and its derivatives (X-saloH) are known to coordinate strongly to metal complexes and adopt a variety of geometries [7–9] as well as coordination modes with the most common being chelating bidentate [10]. From a biological point of view, the saloH derivatives present antibacterial properties [11,12]. We have initiated in our laboratory the synthesis and characterization of transition metal complexes, coordinated to substituted salicylaldehyde and benzophenone ligands [13–15] and studied their interaction with calf-thymus (CT) DNA. Previous studies showed that zinc(II), copper(II), cadmium (II) and nickel(II) complexes of substituted salicylaldehydes or

* Corresponding authors.
E-mail addresses: ariadnezianna@gmail.com (A. Zianna), gepsomas@chem.auth.gr (G. Psomas).

https://doi.org/10.1016/j.jinorgbio.2019.02.013
Received 30 September 2018; Received in revised form 21 February 2019; Accepted 23 February 2019
Available online 24 February 2019
0162-0134/

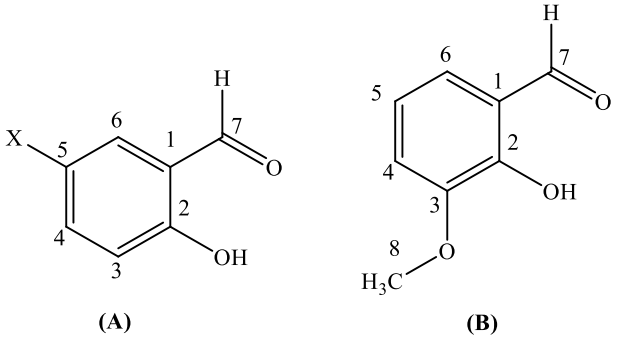

Fig. 1. Molecular structure of the ligands (A) 5-X-saloH (X = NO_2, −Cl, or Br) and (B) 3-OCH_3-saloH used in the present work with the carbon atom numbering.

benzophenones presented interesting results concerning their binding to CT DNA [10,16–22].

As a continuation of our research, we have investigated the synthesis, characterization and biological activity of palladium(II) complexes with X-saloH ligands (X = 3-OCH_3, 5-NO_2, 5-Cl or 5-Br) (Fig. 1). The complexes formulated as [Pd(3-OCH_3-salo)$_2$] **1**, [Pd(5-NO_2-salo)$_2$] **2**, [Pd(5-Cl-salo)$_2$] **3** and [Pd(5-Br-salo)$_2$] **4**, were characterized by physicochemical and spectroscopic techniques (IR, UV–vis) and single-crystal X-ray crystallography (for complex **1**). The CT DNA-binding mode of the complexes was investigated by (i) UV–vis spectroscopy (the DNA-binding constants of the complexes (K_b) were also determined), (ii) DNA-viscosity measurements and (iii) competitive DNA-binding studies with the classic intercalator ethidium bromide (EB) monitored by fluorescence emission spectroscopy. Additionally, the affinity of complexes **1–4** for human (HSA) and bovine serum albumin (BSA) was studied by fluorescence emission spectroscopy and the corresponding binding constants were determined. Furthermore, *in silico* approaches with the employment of molecular docking simulations on the crystal structure of CT DNA and the target serum albumin proteins HSA and BSA aimed to explore the ability of complexes **1–4** to bind to these macromolecules.

2. Experimental

2.1. Materials - instrumentation - physical measurements

The substituted salicylaldehydes (X-saloH), Pd(CH_3COOH)$_2$, CH_3ONa, trisodium citrate, NaCl, CT DNA and EB were obtained as reagent grade from Sigma-Aldrich Co. and used as received. Solvents for the preparation and physical measurements of "extra pure" were obtained from Merck without further purification. DNA stock solution was prepared by dilution of CT DNA to buffer (containing 150 mM NaCl and 15 mM trisodium citrate at pH 7.0) followed by exhaustive stirring at 4 °C for 3 days, and kept at 4 °C for no longer than ten days. The stock solution of CT DNA gave a ratio of UV absorbance at 260 and 280 nm (A_{260}/A_{280}) of 1.88–1.90, indicating that the DNA was sufficiently free of protein contamination [23]. The DNA concentration per nucleotide was determined by the UV absorbance at 260 nm after 1:20 dilution using $\varepsilon = 6600\ M^{-1}\,cm^{-1}$ [24].

Infrared (IR) spectra (400–4000 cm^{-1}) were recorded on a Nicolet FT-IR 6700 spectrometer with samples prepared as KBr pellets. UV–visible (UV–vis) spectra of the compounds as nujol mulls or in DMSO solution (in the range 1×10^{-5} - 5×10^{-3} M) were recorded on a Hitachi U-2001 dual beam spectrophotometer. ^{1}H NMR spectra were recorded at 300 MHz on a Bruker AVANCE III 300 spectrometer using DMSO-d_6 as solvent. C, H and N elemental analyses were performed on a PerkinElmer 240B elemental microanalyzer. Molecular conductivity measurements of 1 mM DMSO solution of the complexes were carried out with a Crison Basic 30 conductometer. Fluorescence spectra were recorded in solution on a Hitachi F-7000 fluorescence spectrophotometer. Viscosity experiments were carried out using an ALPHA L Fungilab rotational viscometer equipped with an 18 mL LCP spindle and the measurements were performed at 100 rpm.

2.2. Synthesis of the complexes 1–4

Complexes **1–4** were prepared according to the published procedure [16], by the addition of an CH_3CN solution (15 mL) of the corresponding X-saloH (1 mmol), deprotonated by CH_3ONa (1 mmol, 54 mg), to an CH_3CN solution (15 mL) of Pd(CH_3COOH)$_2$ (0.5 mmol, 112 mg) at room temperature. The reaction mixture was stirred for 1/2 h and then turned into red-orange.

[Pd(3-OCH_3-salo)$_2$], 1: Red crystals suitable for X-ray structure determination (yield 50%, 204 mg) were filtered off and analyzed as [Pd(3-OCH_3-salo)$_2$], ($PdC_{16}H_{14}O_6$) (MW = 408.70): C: 47.02, H: 3.45%; found: C: 47.08, H: 3.42%. IR spectrum (KBr), selected peaks in cm^{-1}: 1612(strong (s)) ν(C=O), 1324(strong-to-medium (sm)) ν(C-O → Pd), 526(medium (m)) ν(Pd−O). UV–vis spectra: nujol mull, λ/nm: 334, 401; in DMSO, λ/nm ($\varepsilon/M^{-1}\,cm^{-1}$): 335 (5500), 400(shoulder (sh)) (4500). Λ_M (1 mM DMSO) = 11 mho·cm^2·mol^{-1}. ^{1}H NMR in DMSO-d_6, δ (ppm): 10.10 (2H, s, H^7), 8.29 (2H, s, H^6), 7.85 (2H, d, J = 9.0 Hz, H^4), 6.48 (2H, d, J = 9.0 Hz, H^5), 3.60 (6H, s, OCH_3).

[Pd(5-NO_2-salo)$_2$], 2: Orange microcrystalline product was collected (yield 45%, 198 mg) analyzed as [Pd(5-NO_2-salo)$_2$], ($PdC_{14}H_8N_2O_8$) (MW 438.64): C: 38.33, H: 1.83, N: 6.38%; found: C: 38.33, H: 1.81, N: 6.39%. IR spectrum (KBr): selected peaks in cm^{-1}: 1618(s) ν(C=O), 1321(sm) ν(C-O → Pd), 521(m) ν(Pd−O), UV–vis spectra: nujol mull, λ/nm: 366, 424; in DMSO, λ/nm ($\varepsilon/M^{-1}\,cm^{-1}$): 368 (5000), 425 (6000). Λ_M (1 mM DMSO) = 6 mho·cm^2·mol^{-1}. ^{1}H NMR in DMSO-d_6, δ (ppm): 10.09 (2H, s, H^7), 8.23 (2H, broad, H^6), 7.85 (2H, broad, H^4), 6.49 (2H, broad, H^3).

[Pd(5-Cl-salo)$_2$], 3: Orange microcrystalline product was obtained (yield 55%, 231 mg) analyzed as [Pd(5-Cl-salo)$_2$] ($PdC_{14}H_{10}Cl_2O_4$) (MW = 419.56): C: 40.08, H: 2.40%; found: C: 40.10, H: 2.38%. IR spectrum (KBr): selected peaks in cm^{-1}: 1618(s) ν(C=O), 1319(sm) ν(C-O → Pd), 510(m) ν(Pd−O), UV–vis spectra: nujol mull, λ/nm: 334, 422; in DMSO, λ/nm ($\varepsilon/M^{-1}\,cm^{-1}$): 335(sh) (7500), 423(6000); Λ_M (1 mM DMSO) = 13 mho·cm^2·mol^{-1}. ^{1}H NMR in DMSO-d_6, δ (ppm): 9.96 (2H, s, H^7), 7.15 (2H, s, H^6), 6.96 (2H, d, J = 9.2 Hz, H^4), 6.36 (2H, d, J = 9.2 Hz, H^3)

[Pd(5-Br-salo)$_2$], 4: Orange microcrystalline product was collected (yield 53%, 270 mg) analyzed as [Pd(5-Br-salo)$_2$], ($PdC_{14}H_{10}Br_2O_4$) (MW = 508.46): C: 33.07, H: 1.98%; found: C: 33.09, H: 2.00%. IR spectrum (KBr): selected peaks in cm^{-1}: 1612(s) ν(C=O), 1315(sm) ν(C-O → Pd), 513(m) ν(Pd−O), UV–vis spectra: nujol mulls, λ/nm: 318, 422; λ/nm ($\varepsilon/M^{-1}\,cm^{-1}$) in DMSO: 320(sh) (7000), 422(6000). Λ_M (1 mM DMSO) = 12 mho·cm^2·mol^{-1}. ^{1}H NMR in DMSO-d_6, δ (ppm): 9.92 (2H, s, H^7), 7.26 (2H, s, H^6), 7.03 (2H, d, J = 9.0 Hz, H^4), 6.30 (2H, d, J = 9.0 Hz, H^3).

2.3. X-ray crystal structure determination

Single-crystal of [Pd(3-OCH_3-salo)$_2$] **1** suitable for crystal structure analysis was obtained by slow evaporation of the mother liquid at room temperature. It was mounted at room temperature on a Bruker Kappa APEX2 diffractometer equipped with a triumph monochromator using Mo Kα radiation. Unit cell dimensions were determined and refined by using the angular settings of at least 200 high intensity reflections ($> 10\ \sigma(I)$) in the range $11 < 2\theta < 36°$. Intensity data were recorded using ϕ and ω scans. All crystals presented no decay during the data collection. The frames collected for the crystal were integrated with the Bruker SAINT Software package [25], using a narrow-frame algorithm. Data were corrected for absorption using the numerical method (SADABS) based on crystal dimensions [26]. The structures was solved

using the SUPERFLIP package [27], incorporated in Crystals. Data refinement (full-matrix least-squares methods on F^2) and all subsequent calculations were carried out using the Crystals version 14.40b program package [28]. All non-hydrogen atoms were refined anisotropically. Hydrogen atoms were located by difference maps at their expected positions and refined using soft constraints. By the end of the refinement, they were positioned geometrically using riding constraints to bonded atoms. Illustrations with 50% ellipsoids probability were drawn by CAMERON [29]. Crystallographic data for complex **1** are presented in Table S1.

2.4. DNA-binding studies

In order to study the interaction of DNA with the complexes, the compounds were initially dissolved in DMSO (1 mM). Mixing of such solutions with the aqueous buffer DNA solutions used in the studies never exceeded 5% DMSO (v/v) in the final solution, which was needed due to low aqueous solubility of most compounds. In all experiments, the effect of DMSO on the data has been taken into consideration and the appropriate corrections have been performed.

2.4.1. Study with UV–vis spectroscopy

The interaction of complexes **1–4** with CT DNA was studied by UV–vis spectroscopy as a means to investigate the possible binding mode to CT DNA and to calculate the DNA-binding constants (K_b). Control experiments with 5 % DMSO were performed and no changes in the spectra of CT DNA were observed. The UV spectra of a CT DNA solution (0.15–0.22 mM) have been recorded DNA concentration in the presence of each complex at diverse [complex]/[DNA] mixing ratios (= *r*). The DNA-binding constant of the complexes, K_b (in M^{-1}), was determined by the Wolfe-Shimer equation (eq. S1) [30,31] and the plots [DNA]/(ε_A-ε_f) *versus* [DNA] using the UV–vis spectra of the complex (50–100 μM) recorded in the presence of DNA for diverse [DNA]/[complex] mixing ratios (= *r'*). The binding constant to DNA was also determined by using the Scatchard equation (eq. S2) modified for UV–vis spectroscopic titrations [32,33].

2.4.2. Viscometry

The viscosity of DNA ([DNA] = 0.1 mM) in buffer solution (150 mM NaCl and 15 mM trisodium citrate at pH 7.0) was measured in the presence of increasing amounts of the compounds (up to $r = 0.36$). All measurements were performed at room temperature. The obtained data are presented as $(\eta/\eta_0)^{1/3}$ *versus r*, where η and η_0 is the viscosity of DNA in the absence and in the presence of the compound, respectively.

2.4.3. EB-competitive

The competitive studies of each compound with EB were investigated by fluorescence spectroscopy in order to examine whether the compound can displace EB from its EB-DNA conjugate. The EB-DNA conjugate was prepared by adding 20 μM EB and 26 μM CT DNA in buffer (150 mM NaCl and 15 mM trisodium citrate at pH 7.0). The possible intercalating effect of complexes **1–4** was studied by adding a certain amount of a solution of the complex step-wise into a solution of the DNA-EB complex [34]. The influence of the addition of each complex to the DNA-EB solution was monitored by recording the variation of fluorescence emission spectra with excitation wavelength at 540 nm. Complexes **1–4** did not show any fluorescence emission bands at room temperature in solution or in the presence of DNA under the same experimental conditions. Furthermore, the complexes did not interact with EB. After subtracting the negligible effect of DMSO to the fluorescence intensity, the percentage of fluorescence intensity was plotted *versus* the concentration of each compound. The concentration of the added compound required to reduce the fluorescence of the EB-DNA conjugate to 50% (C_{50}) and the apparent DNA-binding constants (K_{app}) of the complexes were calculated according to eq. S3 [35]. The Stern-Volmer constants (K_{SV}, in M^{-1}) were used to evaluate the quenching efficiency for each compound and were calculated from the slope of plots Io/I *versus* concentration of the complex.

2.5. Interaction with serum albumins

The serum albumin (SA)-binding study was performed by tryptophan fluorescence quenching experiments using BSA (3 μM) or HSA (3 μM) in buffer (containing 1 mM trisodium citrate and 150 mM NaCl at pH 7.0). The quenching of the emission intensity of tryptophan residues of BSA at 343 nm or HSA at 351 nm was monitored using complexes **1–4** as quenchers with increasing concentration. The fluorescence emission spectra were recorded from 300 to 500 nm at an excitation wavelength of 295 nm [36]. Most of the compounds exhibited under the same experimental conditions (*i.e.* excitation at 295 nm) a low-intensity emission band in the region 395–415 nm. Therefore, the quantitative studies of the SA-fluorescence emission spectra were performed after subtracting the fluorescence emission spectra of the compounds. The influence of the inner-filter effect [37] on the measurements was evaluated by eq. S4. The plots Io/I *versus* the concentration of the complex and eq. S5 were used to calculate the Stern-Volmer constant (K_{SV}, in M^{-1}) and the SA-quenching constant (k_q, in $M^{-1}\,s^{-1}$). The Scatchard equation (eq. S6) [38] and plots were used to the SA-association constant (K, in M^{-1}) and the number of binding sites per albumin (n) (Tables S2 and S3).

2.6. In silico computational methods (molecular modeling and docking calculations)

Complexes **1–4** were built in 3D coordinates and the best most stable (lowest energy) conformation was detected by geometrical optimization of each structure in the gas phase, as implemented in the Spartan'14 Molecular Modeling program suite [39]. The structure of each molecule was initially optimized (*via* energy minimization) by conformational search using the Monte Carlo method with the MMFF94 molecular mechanics model, included in the Spartan'14 program suite. Geometry optimization (leading to the most stable conformer with the lowest energy) was accomplished *via* quantum-chemical calculations by utilizing the *ab initio* Hartree-Fock method with a 6-31G* basis set. In order to investigate the geometry of the Pd complexes with the most stable isomer for all compounds, Density Functional Theory (DFT) level of quantum chemical calculations were carried out, employing B3LYP hybrid functional which was used for all kinds of atoms. The Becke three-parameter exact exchange functional (B3) [40] combined with the gradient-corrected correlation functional of Lee-Yang-Parr (LYP) [41] of DFT methods, implementing the 6-31G* basis set [42] was employed to optimize the molecules. DFT is an important tool in computational quantum chemical research [43–45]. The geometries were obtained from all-electron calculations. DFT calculations were performed using the Spartan'14 program suite. Initially, HF calculations were employed for optimizing the complexes' structures, preparing them for the docking procedure (a computation level which is more than enough for this kind of simulation). For the study of energetics and geometry optimization, DFT gives better results than the HF calculations on transition metal complexes. For this reason, DFT was the method of choice, conducting also frequency calculations to ensure optimizations are true minima. None of the optimized structures gave imaginary frequencies.

The molecular docking study was carried out on the crystal structure of HSA and BSA target proteins (Protein Data Bank, PDB entry codes 2BXG and 4OR0, respectively), to investigate the effect of the synthesized compound on these proteins. X-ray structures of the HSA protein in complex with bound co-crystallized drug ibuprofen (IBP, 2-(4-isobutylphenyl)propionic acid) [46] and BSA protein in complex with bound co-crystallized drug naproxen (NPS, (*S*)-2-(6-methoxynaphthalen-2-yl)propanoic acid) [47] were obtained from the Brookhaven Protein Data Bank (operated by the Research Collaboratory for

Structural Bioinformatics, RCSB) [48–50]. The chosen crystal structures of HSA and BSA has been refined at 2.70 Å and 2.58 Å resolution, conjugated with IBP and NPS, respectively. For the docking calculations, only the A chains of the proteins were used since chain B is replicate, with IBP and NPS bound at the same ligand binding site among the chains. For this reason, the data for chain B and of each drug referring to this chain were deleted from corresponding PDB files.

Additional molecular docking studies were performed on the crystal structure of CT DNA. We used the determined X-ray crystallographic structure of CT DNA (PDB accession number 1BNA). It was chosen the crystal structure of the synthetic DNA dodecamer d (CpGpCpGpApApTpTpCpGpCpG) which has been refined at 1.9 Å resolution [51].

The molecular docking simulation was performed in project leader of BioMedCAChe 7.5 computer-aided chemistry software package, which is part of the CAChe package (CAChe WorkSystem Pro version 7.5.0.85, Fujitsu Co. Ltd., Tokyo, Japan). BioMed CAChe engages a stochastic optimization method to enhance the intra-molecular energy of a ligand by rotation and analyzing various orientations. BioMed CAChe automates the docking of ligand into active or binding sites by using a genetic algorithm with a fast, simplified potential mean force (PMF). The potential of mean force is a knowledge based approach that extracts pairwise atomic potentials from structure information of known protein-ligand complexes contained in the PDB.

Docking was carried out at full rotation allowing full flexibility for the ligand while keeping the target protein and DNA positions fixed in space. Docking parameters involved steric scan, final search for ligand binding site and refinement of the complex. CAche docking score performs force fields which includes terms as bond stretching, angle bending, torsional, and nonbonded interactions such as Vander Waals and Hydrogen bond interactions. The molecule-based scoring function is made up of four components: 1. Protein-ligand H-bond energy (external H-bond). 2. Protein-ligand van der Waals energy (external vdw). 3. Ligand internal van der Waals energy (internal vdw). 4. Ligand intramolecular H-bond energy (internal H-bond). Docking Score = S (hb_ext) + S (vdw_ext) + S (hb_int) + S (vdw_int). The produced compound-protein conjugates were ranked by the energy score, including their binding conformations. Best docked poses, with both lower binding energies and stronger interaction pattern, were derived from a number of solutions (docking results), usually with the higher ranking. A more rigorous docking function for the final pose selection/ranking of ligands (scoring procedure) was adopted for the best scored lead compound (recalculation of the energy of the top scoring poses in order to improve the selectivity between the lead compounds). This refinement of the scoring poses was necessary in order to minimize the number of false positive and false negative ligands.

Three-dimensional (3D) models of the above protein crystal structures were developed, after the deletion of the co-crystallized bound inhibitor. The final output of the docking procedure is a set of solutions (docking results) ranked according to the corresponding scoring function values, each defined by the 3D coordinates of its atoms and expressed as a PDB file. In this study, the docking procedure with the aid of BioMedCAChe was shown to accurately reproduce experimentally observed binding modes of IBP and NPS, in terms of RMSD (root-mean squared deviation). The BioMedCAChe provided excellent results as low values of RMSD (best docked solutions of docking results 0.23 Å and 0.29 Å, respectively) were observed between the experimental and the best-scoring docked structures derived by superimposition of these structures (the accuracy of the docking results are good when the RMSD is mostly below 1.0 Å). The ability to accurately predict the binding conformation of the enzyme inhibitor and substrate, gave confidence that the BioMedCAChe would also exhibit a similar accuracy with the investigated molecules in the study. The PyMol Molecular Graphics System (Schrödinger, LLC. version 1.8.2.0, www.pymol.org), was used to visualize the molecules and the results of the docking and to construct the molecular models [52].

3. Results and discussion

3.1. Synthesis-general considerations of the complexes

The reaction of $Pd(CH_3COO)_2$ with deprotonated X-saloH (X = 3-OCH_3, 5-NO_2, 5-Cl, or 5-Br) (by CH_3ONa) in acetonitrile led to the formation of complexes **1–4**, according to the reaction:

$Pd(CH_3COO)_2 + 2(X\text{-saloH}) + 2CH_3ONa \rightarrow [Pd(X\text{-salo})_2] + 2CH_3OH + 2CH_3COONa$.

The obtained palladium(II) complexes are neutral (molar conductivity in DMSO solution was found 6–13 $mho{\cdot}cm^2{\cdot}mol^{-1}$) [53] and possess an 1:2 metal-to-(X-salo) composition, as it is indicated from elemental analyses. All complexes are soluble in DMSO and DMF, but insoluble in most organic solvents and H_2O.

Evidence of the coordination mode of the ligands in the palladium complexes has also arisen from the interpretation of the IR and UV–vis spectra. The crystal structure of complex **1** was further *v*erified by single-crystal X-ray crystallography analysis.

3.2. Spectroscopic characterization of the complexes

Infrared spectroscopy has confirmed the deprotonation of the X-saloH ligands and their binding mode. In the IR spectra of complexes **1–4**, the peaks of the stretching and bending vibrations of the phenolic OH around 3200 cm^{-1} and 1400 cm^{-1}, respectively, disappeared indicating the deprotonation of the salicylaldehyde. The band of the free salicylaldehydes at ~1660 cm^{-1} attributable to the carbonyl bond *ν* (C=O), is shifted upon coordination to lower wavenumbers at ~1620 cm^{-1}, denoting the coordination of the X-salo ligand through the carbonyl oxygen. Additionally, the bands originating from the C—O stretching vibrations at 1258–1285 cm^{-1} exhibit in the IR spectra of the complexes positive shifts towards 1315–1324 cm^{-1} denoting coordination through the carbonyl oxygen of the ligand [54,55].

Square-planar palladium(II) complexes are expected to present three d-d type electronic transactions which are attributed to the transitions from the ground state to the excited $^1A_{2g}$, $^1B_{1g}$ and $^1E_{1g}$, respectively, and are expected at 460–520, 405–420 and 320–380 nm, respectively. In all palladium complexes, the first two transitions overlap, and as a result one peak is observed at 400–425 nm. The UV–vis spectra of the complexes have been recorded as nujol mull and in DMSO solution and are similar, suggesting that the complexes retain their structure in solution within the timeframe used for the biological experiments.

^1H NMR spectroscopy was also used in order to confirm deprotonation of salicylaldehyde and the stability of the complexes in solution. The deprotonation of the phenolic hydrogen can be easily concluded from the absence of the –OH signal, which is observed in the ^1H NMR spectra of the free X-saloH, appearing as single peak at δ = 12 ppm. All signals are slightly shifted as expected upon binding to palladium ion. The ^1H NMR spectra of the complexes give the protons, attributable to the aldehydo group at δ = 9.92–10.10 ppm. The absence of additional set of signals related to dissociated ligands suggests that all complexes remain intact in solution. The ^1H NMR spectrum of complex $[Pd(5\text{-Cl-salo})_2]$ is representatively shown in Fig. 2.

3.3. Structure of the complexes

3.3.1. Description of the crystal structure of complex 1

The molecular structure of complex $[Pd(3\text{-}OCH_3\text{-salo})_2]$, **1** has been verified by X-Ray crystallography and is shown in Fig. 3. The complex is centrosymmetric with Pd1 atom on the inversion center. In the crystal structure of complex **1**, the deprotonated 3-OCH_3-salo ligands are coordinated to the palladium ion in a chelating bidentate mode through the carbonyl oxygen O1 and the deprotonated phenolato oxygen O2 (O1-Pd1-O2 = 94.36(8)°). The coordination number of Pd is four and the geometry around is square planar. The Pd1-$O2_{phenol}$ bond distance

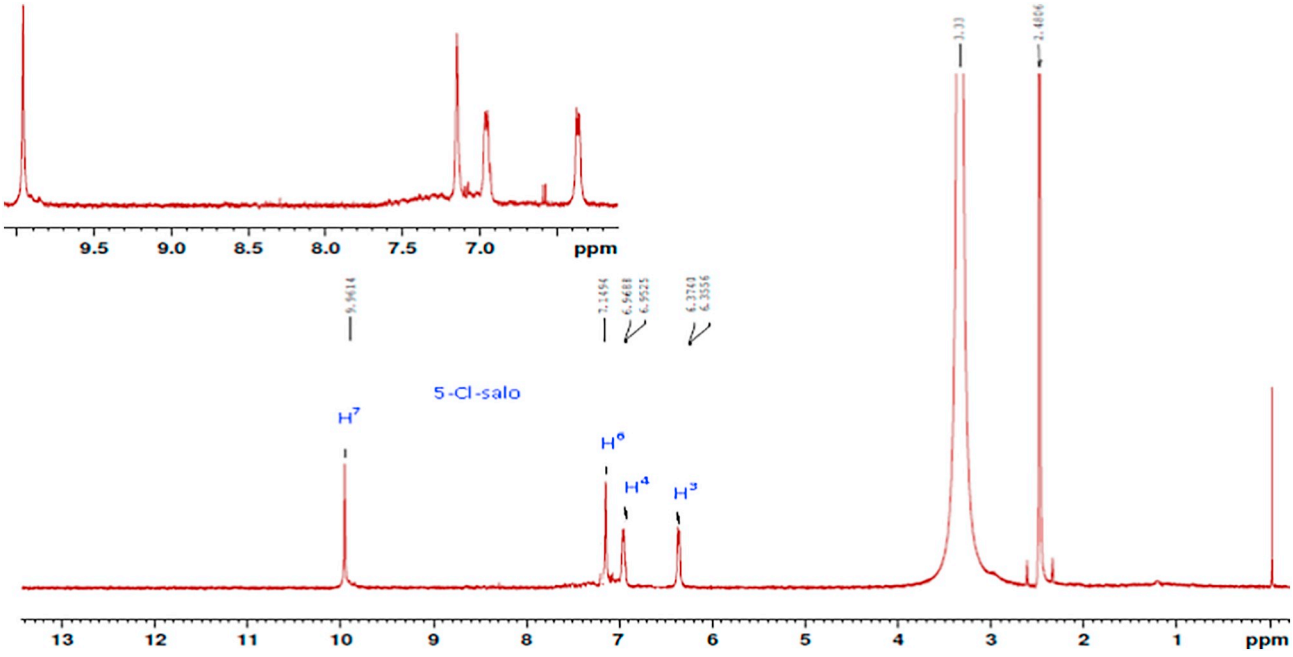

Fig. 2. ^{1}H NMR spectrum of complex [Pd(5-Cl-salo)$_2$] in DMSO-d_6.

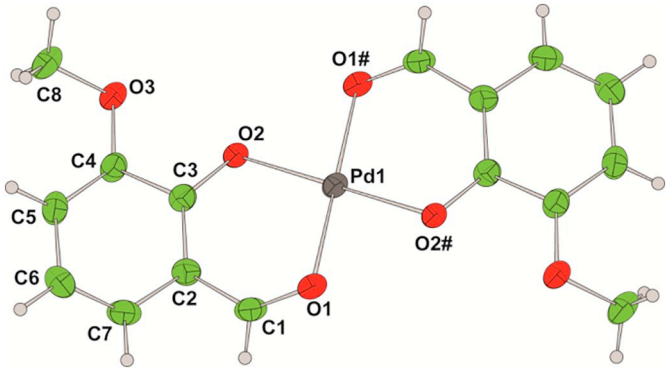

Fig. 3. Molecular structures of complex **1** with the displacement ellipsoids shown at the 50% probability level.

(Pd1-O2 = 1.9775(19) Å) is almost equal to the Pd1-O1$_{carbonyl}$ bond distance (Pd1-O1 = 1.981(2) Å) and comparable to those of complex [Pd(salo)$_2$] found in the literature [56]. However, in most salicylaldehyde metal complexes the M-O$_{phenol}$ bond is longer than the M-O$_{carbonyl}$ bond [8,15–19]. The structure is further stabilized by the existence of intermolecular π-π stacking interactions originating from 3-OCH$_3$-salo ligands of two neighboring molecules being in a centroid-to-centroid distance of 3.52 Å.

3.3.2. Proposed structures for complexes 2–4

Based on the experimental data (IR, UV–vis spectroscopy, elemental analysis, molar conductivity) and a comparison with the already structurally characterized palladium complex found in the literature [56], we may propose a structure for complexes **2–4**. These complexes are expected to have similar structure with the reported [Pd(salo)$_2$] [56], as well as with complex **1** which is structurally characterized in the present work, exhibiting thus a square planar geometry with the two deprotonated 5-X-salicylaldehydato ligands bidentately coordinated to the palladium, most probably in a *trans* arrangement.

The fully-optimized structures with DFT calculations revealed that the *trans* orientation of the O atoms around Pd is the most stable for each complex. Generally, the isomeric complexes were proved to have close relative electronic energies because of the similar structural geometries. The more favorable structures observed are those with *trans* arrangement, giving rise to lower minimal energies of complexes **1–4** with values of −1196.197627, −1376.202744, −1886.381602 and -6152.8918721 hartrees, respectively, compared to *cis* arrangement with values of −1196.102587, −1376.189994, −1886.132311 and -6152.8907380 hartrees, respectively. The accuracy of the DFT method was verified by comparing the most stable isomer geometry for complex **1**, with the one derived from the experimental X-ray crystallography. In this way, the proposed structures of complexes **2–4** were found to be reliable.

3.4. Interaction with calf-thymus DNA

Metal complexes may interact with CT DNA covalently and/or non-covalently. In covalent interactions, at least one labile ligand of the complexes is replaced by a nitrogen atom of a DNA-base (*i.e.* guanine-N7). In non-covalent interactions which usually occur in the case of stable metal complexes, the metal complexes may interact to DNA *via* three main types: (i) intercalation through π-π stacking of the complex in-between DNA-base pairs, (ii) groove-binding to the major and/or minor groove through van der Waals interactions and hydrogen bonding and (iii) electrostatic interaction to the external phosphate groups of the DNA-helix *via* Coulomb forces [57,58].

3.4.1. DNA-binding studies by UV–vis spectroscopy

UV–vis spectroscopy can be preliminarily used to investigate the existence of interaction between a compound and CT DNA and to calculate its binding strength. The band of CT DNA at 258–260 nm is due to the π➔π* transition of the DNA bases. Any type of interaction between DNA and the tested compounds, *i.e.* destruction of hydrogen bonds between complementary bases, stacking pattern changes, covalent binding or intercalation, may perturb this band of CT DNA or the intra-ligand transition bands of the complex during these titrations [58].

The UV–vis spectra of a DNA solution were recorded in the presence of complexes **1–4** at increasing *r* values (representatively shown for complex **4** in Fig. S1). Addition of the compounds into DNA solution resulted in slight hyperchromism of the DNA band at 258 nm, which may be assigned to the formation of a new adduct of the compounds

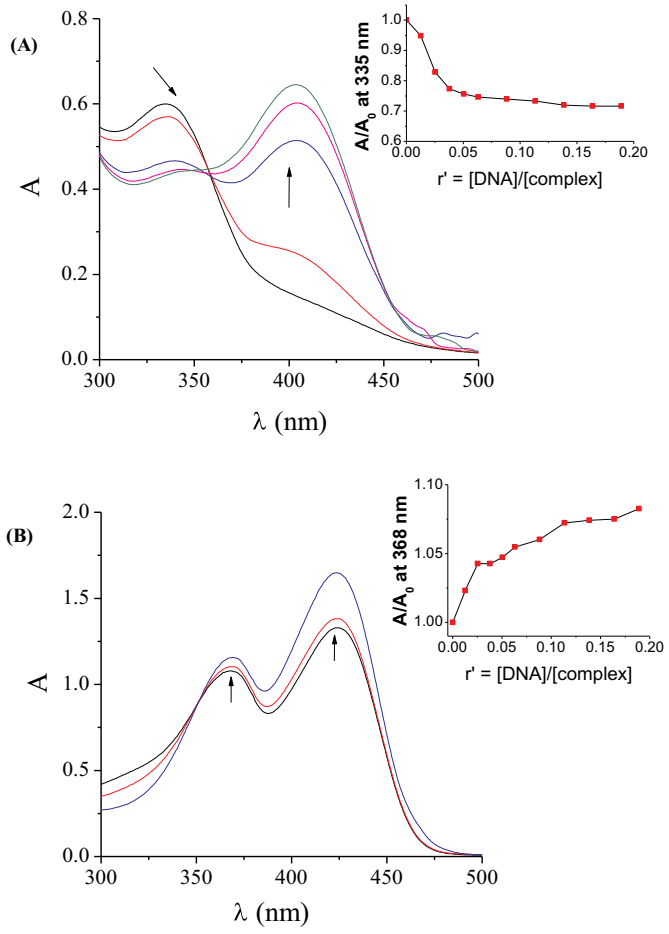

Fig. 4. UV–vis spectra of DMSO solution of complex (**A**) [Pd(3-OCH_3-salo)$_2$] (10^{-4} M) and (**B**) [Pd(5-NO_2-salo)$_2$] (5×10^{-5} M) in the presence of increasing amounts of CT DNA (r' = [DNA]/[complex] = 0–0.2). The arrows show the changes upon increasing amounts of CT DNA. (Insets: The changes of A/A_0 *versus* r').

with double-helical DNA [59]. Moreover, in the UV–vis spectra of complex **1** (Fig. 4(A)) in the presence of increasing amounts of CT DNA, the two observed intraligand bands at 335 nm (band I) and 400 nm (band II) exhibit a slight hypochromism and intense hyperchromism, respectively, with band I also showing a 10-nm red-shift. In average, similar are the changes observed in the UV–vis spectra of complexes **3** and **4** in the presence of CT DNA (Fig. S2, Table 1). Both intraligand bands in the UV–vis spectra of complex **2** (Fig. 4(B)) present hyperchromism upon addition of CT DNA, without any appreciable shift of the λ_{max}. These spectroscopic features may suggest the binding of the compounds to CT DNA, but the exact binding mode cannot be proposed; therefore, further DNA-viscosity measurements were conducted in order to clarify the DNA-binding mode of the compounds.

The magnitude of the binding strength of a compound with CT DNA may be evaluated through the calculation of the DNA-binding constants values. The K_b constants were obtained by the plots [DNA]/(ε_A-ε_f) *versus* [DNA] (Fig. S3) with the Wolfe-Shimer equation [30] as well as the Scatchard equation (eq. S2) [32,33] and the corresponding plots (fig. S4). In both cases, the K_b constants of complexes **1–4** (Table 1) are relatively high suggesting strong binding of the complexes to CT DNA, with **2** having the highest K_b constant among the complexes. In general, the K_b constants of the complexes have the same magnitude with a series of reported metal complexes with X-salo ligands [16–22] as well as of Pd complexes with derivatives of carboxamides or salicylaldehydes as ligands found in the literature [60,61].

3.4.2. EB-displacement studies

A solution containing the EB-DNA conjugate shows an intense fluorescence emission band at 592 nm (with $\lambda_{excitation}$ = 540 nm) as a result of the intercalation of the planar EB phenanthridine ring in-between adjacent DNA-base pairs; for this reason, EB is considered a typical indicator of intercalation to DNA. If an intercalating compound which can bind to DNA equally or stronger than EB is added into this solution, a significant quenching of the EB-DNA fluorescence emission may be induced [36]. Complexes **1–4** do not show any fluorescence emission bands at room temperature in solution or in the presence of CT DNA or EB under the same experimental conditions ($\lambda_{excitation}$ = 540 nm). Therefore, the changes observed in the fluorescence emission spectra of the EB-DNA solution, when complexes **1–4** are added, may be useful to examine the EB-displacing ability of the complexes [62].

The fluorescence emission spectra of pre-treated EB-DNA ([EB] = 20 μM, [DNA] = 26 μM) were recorded in the presence of increasing amounts of each complex **1–4** up to the value of r = 0.5 (representatively shown for complex **1** in Fig. 5(A)). The addition of the complexes resulted in a significant quenching of the fluorescence emission band of the DNA-EB compound at 592 nm which was up to 66.2% (for **1**) of the initial EB-DNA fluorescence (Fig. 5(B) and Table 2).

Table 1
UV–vis spectroscopic features of free X-saloH and their complexes **1–4** upon addition of DNA. UV–vis band (λ in nm) (percentage of hyper- or hypo-chromism ($\Delta A/A_0$, %), blue- or red- shift of λ_{max} ($\Delta\lambda$, nm)) and the corresponding DNA-binding constants (K_b was calculated by the Wolfe-Shimer equation (eq. S1) and by the Scatchard equation (eq. S2) where n = number of binding sites).

Compound	Band (λ, nm) (($\Delta A/A_0$) (%),[a] $\Delta\lambda$ (nm)[b])	K_b (M^{-1})[f]	K_b (M^{-1})[g]	n[g]
3-OCH_3-saloH [18]	340 (−28, +3); 400(sh) (+ > [c], 0)	9.84(± 0.16) × 10^4	–	–
5-NO_2-saloH [16]	316 (− < [d], nd [e]); 366(+ >, +5); 430(+ > [c], −5)	5.25(± 0.25) × 10^5	–	–
5-Cl-saloH [16]	336 (−64, +4); 424(+ >, −5)	2.59(± 0.11) × 10^7	–	–
5-Br-saloH [16]	336 (−51, +2); 423(+ >, −5)	7.13(± 0.22) × 10^5	–	–
[Pd(3-OCH_3-salo)$_2$], **1**	335 (−28, +10), 400 (+327, 0)	2.68(± 0.13) × 10^6	1.31(± 0.08) × 10^6	0.30
[Pd(5-NO_2-salo)$_2$], **2**	368 (+8, 0), 425 (+25, 0)	4.53(± 0.22) × 10^6	1.61(± 0.21) × 10^6	0.10
[Pd(5-Cl-salo)$_2$], **3**	335 (−39, 0), 423 (+32, 0)	5.13(± 0.95) × 10^5	5.72(± 0.22) × 10^5	0.41
[Pd(5-Br-salo)$_2$], **4**	320 (−43, +14), 422 (+45, −4)	4.90(± 0.12) × 10^5	5.80(± 0.22) × 10^5	0.47

[a] "+" denotes hyperchromism and "-"denotes hypochromism.
[b] "+" denotes red-shift and "-"denotes blue-shift.
[c] "+ >" denotes extreme hyperchromism.
[d] "− <" denotes extreme hypochromism.
[e] "nd" = not determined.
[f] K_b was calculated by the Wolfe-Shimer equation (eq. S1).
[g] K_b and n were calculated by the Scatchard equation (eq. S2).

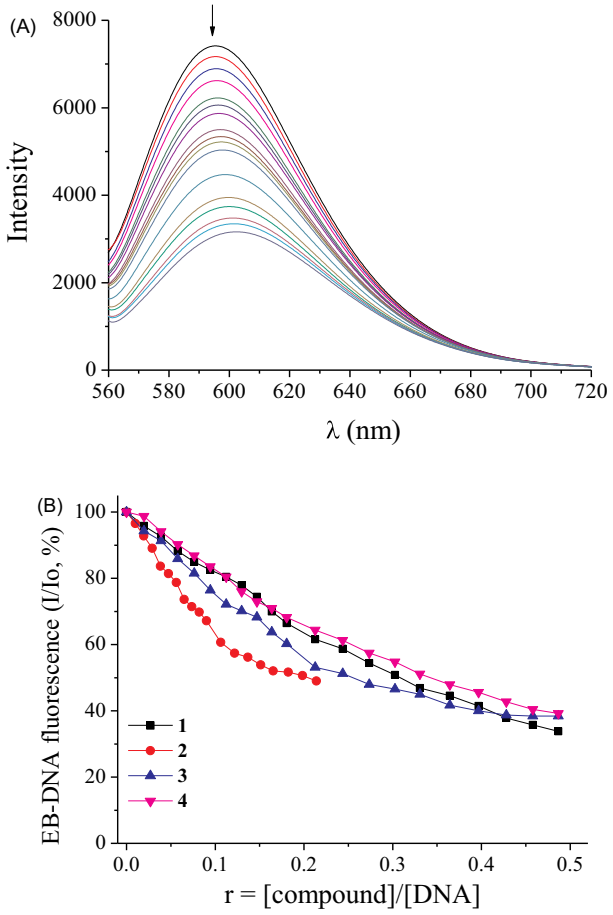

Fig. 5. (A) Fluorescence emission spectra ($\lambda_{excitation}$ = 540 nm) for EB-DNA ([EB] = 20 μM, [DNA] = 26 μM) in buffer solution in the absence and presence of increasing amounts of complex **1** (up to r = 0.5). The arrow shows the changes of intensity upon increasing amounts of **1**. (B) Plot of EB relative fluorescence emission intensity at $\lambda_{emission}$ = 592 nm (I/Io, %) *versus* r (r = [complex]/[DNA]) in the presence of complexes **1–4** (up to 33.8% of the initial EB-DNA fluorescence intensity for **1**, 49.1% for **2**, 38.4% for **3** and 39.2% for **4**).

Table 2
Percentage of EB-DNA fluorescence quenching (ΔI/Io, %), EB-DNA Stern-Volmer constants (K_{SV}, in M^{-1}), C_{50} (in μM) and apparent binding constant (K_{app}, in M^{-1}) for complexes **1–4**.

Compound	ΔI/Io (%)	K_{SV} (M^{-1})	C_{50} (μM)	K_{app} (M^{-1})
[Pd(3-OCH_3-salo)$_2$], **1**	66.2	7.40(± 0.26) × 10^4	15.6	2.95 × 10^6
[Pd(5-NO_2-salo)$_2$], **2**	50.9	1.17(± 0.03) × 10^5	10.3	4.47 × 10^6
[Pd(5-Cl-salo)$_2$], **3**	61.6	7.74(± 0.12) × 10^4	12.8	3.59 × 10^6
[Pd(5-Br-salo)$_2$], **4**	60.8	6.47(± 0.13) × 10^4	17.3	2.66 × 10^6

The ability of the complexes to displace EB for the EB-DNA conjugate may be indicated, revealing, thus, indirectly the interaction with CT DNA by the intercalative mode [34].

From plots in Fig. 5(B), the C_{50} values of complexes **1–4** were determined (Table 2); taking as K_{EB} = 2.3 × 10^6 M^{-1} which has been obtained after applying the Bjerrum–Brönsted equation to adapt the DNA-binding constant of EB reported in literature [63], the values of the corresponding K_{app} (Table 2) were calculated with eq. S3 [35]. The values of K_{app} of complexes **1–4** are in the range of 2.66 × 10^6 M^{-1} to 4.47 × 10^6 M^{-1} showing the ability of the complexes to displace EB from EB-DNA conjugate and suggesting that complexes **1–4** may intercalate into DNA double helix [64,65]. Complex **2** has the highest K_{app} among the complexes, which is in accordance with the K_b values calculated from UV–vis spectroscopy. The plots Io/I *versus* the concentration of the complexes (Fig. S5) illustrate a linear relation of the data. The K_{SV} constants (Table 2) of the complexes as calculated from these plots (Fig. S5) are relatively high suggesting tight binding to DNA, with complex **2** having the highest K_{SV} constant among the complexes.

3.4.3. DNA-binding study with viscosity measurements

The DNA-viscosity is sensitive to DNA-length changes when interacting with a compound since the solution viscosity (η/η_0) and DNA length (L/L_0) are related by the equation $(L/L_0) = (\eta/\eta_0)^{1/3}$ [66,67]. The interaction *via* intercalation (insertion of the compound in-between the DNA-base pairs) will result in an increase of the separation distance of base pairs lying at intercalation sites in order to host the inserting compound, inducing an increase of the length of the DNA-helix and, subsequently an increase of DNA viscosity is observed, the magnitude of which is usually in accordance to the strength of the interaction. In the case of binding to DNA-grooves *via* a partial or non-classic intercalation (*i.e.* electrostatic interaction or external groove-binding), a bend or kink in the DNA-helix may occur leading to a slight shortening of its effective length, and the change in viscosity of the DNA solution is less pronounced or there is no change at all [68]. This characteristic can be proved helpful in clarifying the interaction with DNA.

The viscosity measurements were carried out on CT DNA solutions (0.1 mM) upon addition of increasing amounts of the compounds (up to the value of r = 0.36) at room temperature. The relative DNA-viscosity exhibited an increase upon addition of compounds **1–4,** especially for complex **1** (Fig. 6). Therefore, the behavior of DNA-viscosity in the presence of complexes **1–4** may be considered evidence of the existence of intercalation of the complexes in-between the DNA-bases. From Fig. 6, it may be observed that the DNA-viscosity increases in the order of complexes **1** > **2** > **4** > **3** while the K_b values increase in the order **2** > **1** > **3–4**. From these data, we may conclude that complexes **1** and **2** having higher K_b values may induce higher increase of DNA viscosity than complexes and **3** and **4**, and subsequently higher elongation of DNA helix.

3.5. Interaction with serum albumins

Serum albumins are the major soluble protein constituents of the circulatory system. They have many physiological functions [69] and the most important one is to transport drugs and other bioactive small molecules through the bloodstream [69,70]. BSA has been one of the most extensively albumins studied, especially because of its structural homology with HSA [68]. BSA is constituted of three homologous

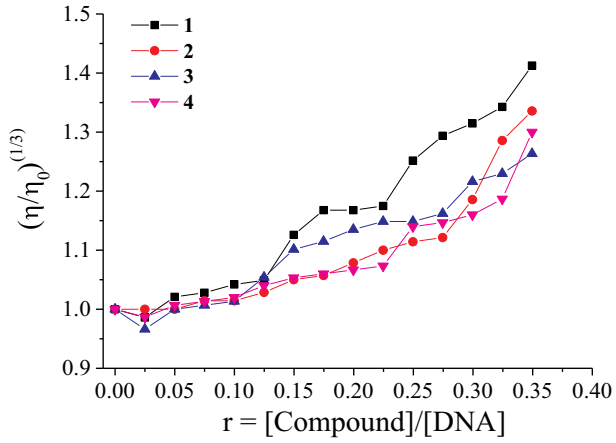

Fig. 6. Relative viscosity $(\eta/\eta_0)^{1/3}$ of CT DNA (0.1 mM) in buffer solution (150 mM NaCl and 15 mM trisodium citrate at pH 7.0) in the presence of complexes **1–4**, at increasing amounts (r = 0–0.36).

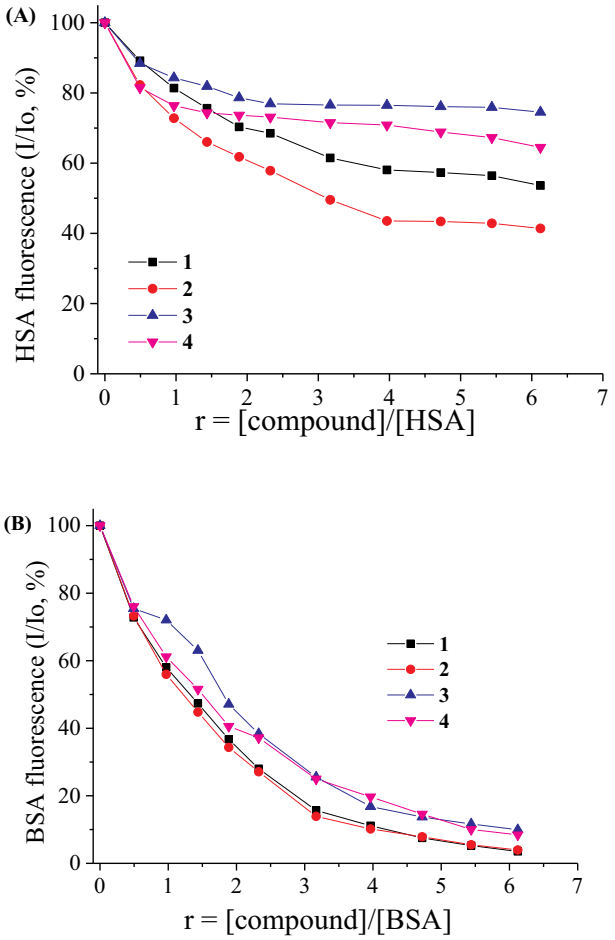

Fig. 7. Plot of relative fluorescence emission intensity (**A**) of HSA at λ_{em} = 351 nm (I/Io, %) *versus r* (*r* = [complex]/[HSA]) for complexes **1–4** (up to 54.6% of the initial HSA fluorescence for **1**, 41.4% for **2**, 74.5% for **3** and 64.5% for **4**), (**B**) of BSA at λ_{em} = 342 nm (I/Io, %) *versus r* (*r* = [complex]/[BSA]) for complexes **1–4** (up to 3.5% of the initial BSA fluorescence for **1**, 4.0% for **2**, 10.0% for **3**, 8.5% for **4**).

domains (I, II, III) and has two tryptophans, Trp-134 and Trp-212, embedded in the first subdomain IB and subdomain IIA, respectively. HSA is a globular protein composed of 585 aminoacid residues in three homologous a-helices domains (I-III) bearing only one tryptophan located at position 214 along the chain, in subdomain IIA [71,72]. Solutions of BSA and HSA exhibit an intense fluorescence emission band with $\lambda_{em,max}$ = 342 nm and 351 nm, respectively, when excited at 295 nm [36], because of the tryptophan residues. Complexes **1–4** in buffer solutions exhibited a maximum emission in the region 395–415 nm under the same experimental conditions and the SA fluorescence emission spectra were corrected before the calculations processing. The inner-filter effect was calculated with eq. S3 and it did not affect the measurements [36,37].

The addition complexes **1–4** to a SA solution resulted in a low-to-moderate quenching of the respective SA fluorescence emission band (*i.e.* at λ_{em} = 351 nm for HSA and at λ_{em} = 342 nm for BSA) which, in the case of BSA, was more pronounced (Fig. 7). Thus, the observed SA-quenching in the presence of a compound may be attributed to changes in tryptophan environment of SA because of possible changes in secondary albumin conformation, subunit association, substrate binding or denaturation resulting from the binding of the compounds to SA [73]. The K_{SV} constants (Tables S2 and S3) were calculated from the slopes in plots Io/I *versus* the concentration of the complexes (Figs. S6 and S7) and the k_q constants of the compounds (Table 3) were calculated with eq. S5. In all cases, the SA-quenching ability of complexes **1–4** is higher than the corresponding free X-saloH ligands, with complex **2** exhibiting the highest k_q constant for HSA and complex **3** for BSA. The k_q constants of the complexes are higher than $10^{10}\,M^{-1}\,s^{-1}$ indicating, thus, the existence of static quenching mechanism and confirming their interaction with the albumins [35].

The K constants of the compounds for both SAs were calculated from the corresponding Scatchard plots (Figs. S8 and S9) and the Scatchard equation for fluorescence titrations (eq. S6) and they are cited in Table 3. The K constants of the complexes are similar to that of the corresponding free X-saloH, with complexes **4** and **2** exhibiting the highest association constants for HSA and BSA, respectively, among the complexes. The SA-binding constants of complexes **1–4** are of the same magnitude with those reported for diverse metal complexes with X-salo ligands [16–22] or other palladium(II) complexes with carboxamides or semicarbazones as ligands reported in the literature [60,61].

The K constants of the complexes are in the range 7.76×10^4 - $9.76 \times 10^5\,M^{-1}$, indicating their tight binding to the SAs in order to get transported towards their potential targets; upon their arrival, the compounds may have the potential to get released, since their non-covalent binding to the SAs is less tighter than the strongest known noncovalent (irreversible) binding attributed to the interaction of diverse ligands to the protein avidin with K value ≈ $10^{15}\,M^{-1}$ [74,75].

3.6. Docking calculations

Binding energies of complexes **1–4** with HSA, BSA and CT DNA are shown in Table 4. From these data, it is obvious that complex **2** seems to succeed better binding (lower binding energy) for both HSA and BSA, followed by complexes **4**, **3**, **1** (for HSA) and **3**, **1**, **4** (for BSA). For DNA binding, all three complexes **1–3** presented similar binding energies. Complex **4** proved to bind with the highest energy.

All molecules are shown to be stabilized inside different binding pockets of HSA and BSA proteins, but at places which have already been reported in the literature (Table 5). From Fig. 8, it is deduced that complex **2** is docked in binding sites II (lower energy, most favorable) and I*V* (higher energy, least favorable) of HSA protein, while IBP is co-crystallized in binding sites III and IV of the protein. The docking pose of complex **2** in binding site V of BSA is illustrated in Fig. 9, with naproxen (NPS) co-crystallized in binding sites II, III and I*V* of the protein. In all docking poses, the secondary structure of HSA with its

Table 3
The quenching (k_q) and binding (K) constants for HSA and BSA calculated for free X-saloH and complexes **1–4**.

Compound	$k_{q(HSA)}$ ($M^{-1}\,s^{-1}$)	$K_{(HSA)}$ (M^{-1})	$k_{q(BSA)}$ ($M^{-1}\,s^{-1}$)	$K_{(BSA)}$ (M^{-1})
5-NO_2-saloH [18]	$5.00(\pm 0.46) \times 10^{12}$	$2.41(\pm 0.09) \times 10^5$	$6.55(\pm 0.17) \times 10^{12}$	$1.25(\pm 0.07) \times 10^5$
3-OCH_3-saloH [18]	$2.52(\pm 0.23) \times 10^{11}$	$1.56(\pm 0.17) \times 10^5$	$2.37(\pm 0.13) \times 10^{12}$	$2.15(\pm 0.10) \times 10^5$
5-Cl-saloH [18]	$5.64(\pm 0.40) \times 10^{11}$	$2.19(\pm 0.10) \times 10^5$	$1.46(\pm 0.06) \times 10^{12}$	$3.11(\pm 0.20) \times 10^4$
5-Br-saloH [18]	$2.31(\pm 0.32) \times 10^{11}$	$1.43(\pm 0.09) \times 10^6$	$4.63(\pm 0.31) \times 10^{12}$	$1.43(\pm 0.08) \times 10^5$
[Pd(3-OCH_3-salo)$_2$], **1**	$6.07(\pm 0.25) \times 10^{12}$	$1.36(\pm 0.05) \times 10^5$	$3.22(\pm 0.22) \times 10^{13}$	$1.69(\pm 0.07) \times 10^5$
[Pd(5-NO_2-salo)$_2$], **2**	$1.04(\pm 0.03) \times 10^{13}$	$1.90(\pm 0.09) \times 10^5$	$3.60(\pm 0.25) \times 10^{13}$	$1.78(\pm 0.05) \times 10^5$
[Pd(5-Cl-salo)$_2$], **3**	$4.57(\pm 0.37) \times 10^{12}$	$4.58(\pm 0.16) \times 10^5$	$5.25(\pm 0.32) \times 10^{13}$	$7.76(\pm 0.51) \times 10^4$
[Pd(5-Br-salo)$_2$], **4**	$2.42(\pm 0.26) \times 10^{12}$	$9.76(\pm 0.42) \times 10^5$	$3.27(\pm 0.17) \times 10^{13}$	$1.58(\pm 0.04) \times 10^5$

Table 4
Global binding energies (in kcal/mol) of complexes **1–4** docked on CT DNA, HSA and BSA targets (PDB accession numbers: 1BNA, 2BXG and 4OR0, respectively).

Complex	CT DNA	HSA	BSA
[Pd(3-OCH_3-salo)$_2$] (**1**)	−40.93	−36.30	−44.54
[Pd(5-NO_2-salo)$_2$] (**2**)	−40.67	−42.32	−51.00
[Pd(5-Cl-salo)$_2$] (**3**)	−40.53	−37.99	−45.97
[Pd(5-Br-salo)$_2$] (**4**)	−38.04	−38.07	−42.61

Table 5
Binding sites of complexes **1–4** docked on HSA and BSA targets (PDB accession numbers: 2BXG and 4OR0, respectively) (* and ** denote common binding site with IBP or NPS, respectively).

Complex	Binding sites of HSA	Binding sites of BSA
[Pd(3-OCH_3-salo)$_2$] (**1**)	III*	I
[Pd(5-NO_2-salo)$_2$] (**2**)	II (lowest energy, most favorable), IV* (highest energy, least favorable)	V
[Pd(5-Cl-salo)$_2$] (**3**)	II	II**
[Pd(5-Br-salo)$_2$] (**4**)	II	II**

subdomains mentioned in Fig. 8 is assigned based on Sugio *et al* [76]. Similarly, the structure of BSA mentioned in Fig. 9 is derived from Bujacz *et al* [41]. From Table 5 and Figs. 8, 9 and S10-S15, it is deduced that complex **1** is anchored in binding site III of HSA and binding site I of BSA, while complexes **3** and **4** are both stabilized inside the cavity of binding site II in both target proteins. Complex **2** is bound in the pocket of binding site II and IV of HSA and binding site V of BSA. From Figs. 8 and S10 it is deduced that complexes **1** and **2** are anchored inside binding sites III (complex **1**) and IV (complex **2**) of HSA, more closely to IBP than complexes **3** and **4**. In the contrary, from Figs. S14 and S15 it is derived that both complexes **3** and **4**, are stabilized inside binding pocket II of BSA at the same place with NPS, which is not the case for complexes **1** and **2** which are bound in sites I and V, respectively, away from the binding pocket of NPS. Binding interactions of complexes **1–4** with amino acid residues of the binding pocket of HSA and BSA are shown in Tables S4–S7. The stabilization of the complexes is succeeded with the formation of hydrogen bonds, hydrophobic and polar interactions, as well as pi-pi interactions. Our models for HSA and BSA complexation with complexes **1–4** suggest that they could be bound at different sites of human serum protein, which accommodates better their transportation.

From Tables 3 and 4 it is deduced that complex **2** (which exhibits the highest association constant for BSA) was found also to bind more stable with BSA showing the lowest binding energy (−51.00 kcal/mol). The ranking of complexes **1–4** for binding constants K and global binding energies, are in the order (highest to lowest binding capacity): **2** > **1** > **4** > **3** and **2** > **3** > **1** > **4**, respectively. For HSA, according to K constants, the most stable binding is achieved by complex **4**, which is second in the binding capacity derived from the calculated binding energies (order for binding energies, from lowest to highest: **2** > **4** > **3** > **1**).

The computed binding energies of the best pose of complexes **1–4** with CT DNA are shown in Table 4. The data propose that complexes **1–3** can be bound more potent to DNA, than complex **4**. From Figs. 10 and S16–S18, it is obvious that all complexes are bound inside the minor groove of DNA, with complexes **2–4** buried deeper in the groove than complex **1**. In addition, Tables S8–S11 are illustrating the nucleotides and the atoms of the complexes involved in the binding interactions, along with bond lengths and type of interaction.

It is deduced that complex **1** exhibited fewer contacts with nucleotides, compared to complexes **2–4**. Our models for predicted

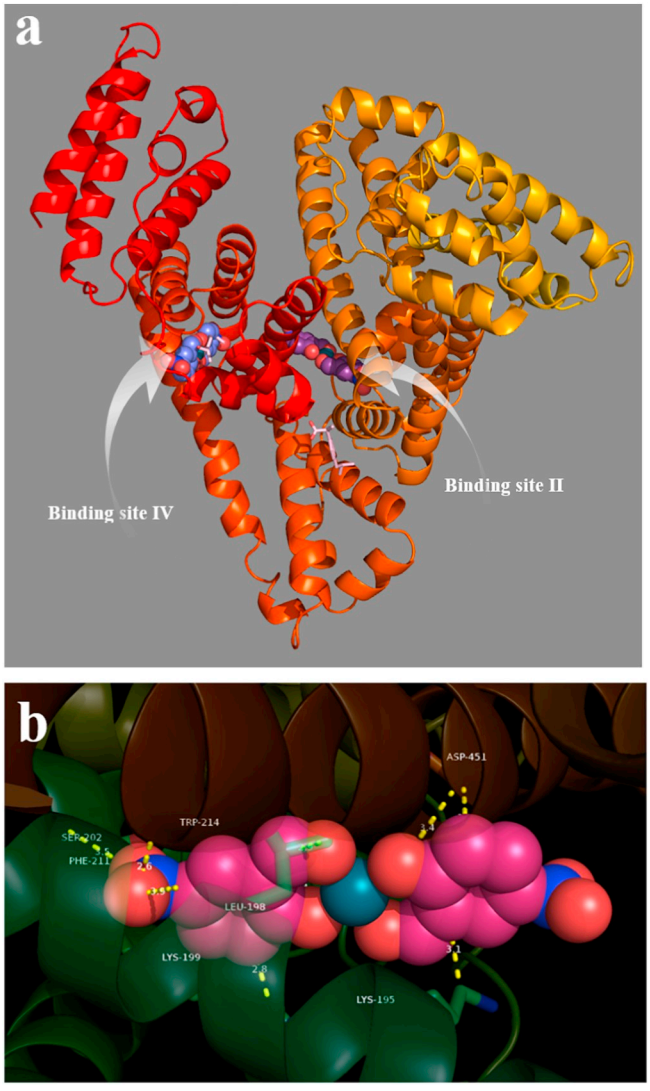

Fig. 8. (a) Docking pose orientation of complex **2** superimposed with ibuprofen (IBP) on HSA target protein (PDB ID: 2bxg). Complex **2** is docked in binding sites II (lower energy, most favorable) and I*V* (higher energy, least favorable). IBP is crystallized in binding sites III and IV of the protein. Complex **2** in binding site II, is bound in a cavity formed by helices IIA-h1, IIA-h6, IIIA-h4, IIIA-h5 and IIA-h2. In binding site IV, accommodating both complex **2** and IBP, the cavity is formed by helices IIIA-h1, IIIA-h5 and IIIA-h6. (b) Ligand binding site II of the protein with the docked complex **2** stabilized with hydrogen bonds with Arg218, Ser202 and Trp214 amino acid residues of the binding cavity. Trp214 is also contributes to the stability of the complex through π-π interactions. Additionally, hydrophobic interactions of complex **2** with the amino acid residues Asp451, Lys195 and Lys199 reinforce the anchorage of the molecule in the binding pocket. Target protein is illustrated as cartoon in depth-cued. Complex **2** is depicted in sphere mode colored according to atom type by magenta C atoms (binding site II) and blue C atoms (binding site IV) and hot-pink C atoms in (b), while co-crystallized IBP is rendered in stick representation and colored according to atom type by light pink C atoms. Hydrogen atoms of ligands are omitted for clarity. Both structures were ray-traced and illustrated with the aid of PyMol Molecular Graphics System.

binding poses of complexes **1–4** into CT DNA suggest intercalation of complexes with A and B helices of DNA, between purines and pyrimidines of the same strand and between strands as well in minor groove. Due to different domain of the DNA taking place in the binding of the complexes, it was found common bound nucleotides only for complexes **3** and **4** (DG10, DC11, DG16 and DA17).

The DNA-binding constants (K_b) reported in Table 1 and calculated

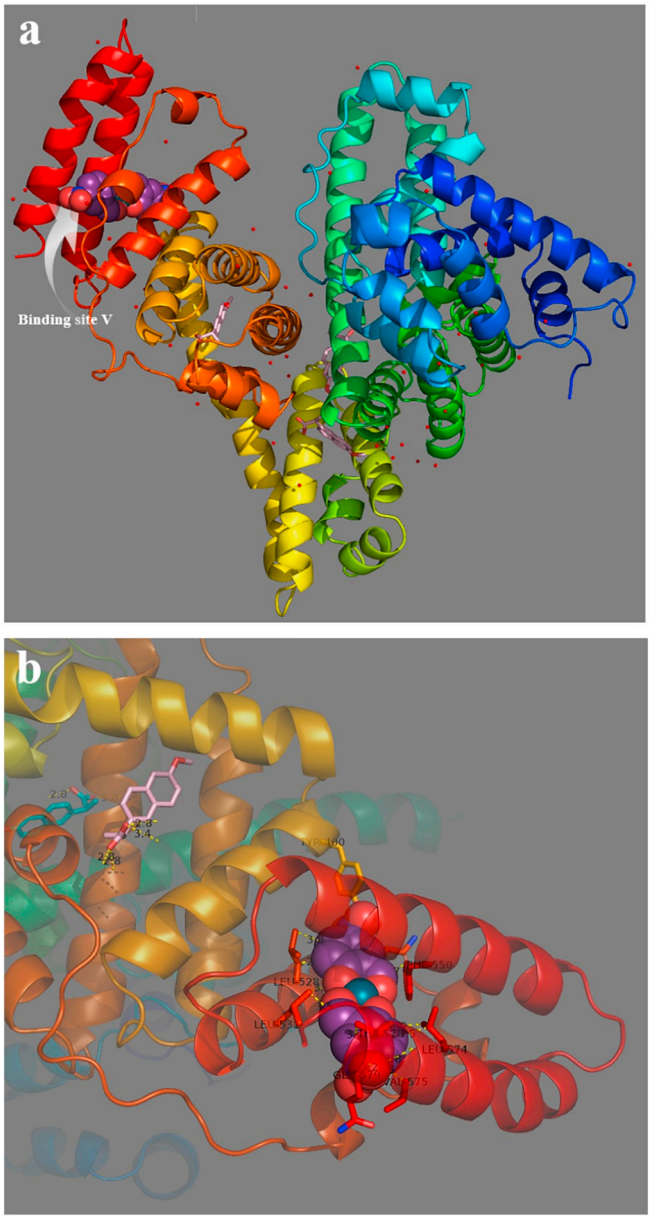

Fig. 9. (a) Docking pose orientation of complex **2** superimposed with naproxen (NPS) on BSA target protein (PDB ID: 4or0). Complex **2** is docked in binding site V, while NPS is crystallized in binding sites II, III and IV of the protein. Complex **2** is bound in a cavity formed by helices IIIB-h2, IIIB-h3 and IIIB-h4. (b) Ligand binding site V of the protein with the docked complex **2** stabilized with the amino acid residues of the binding cavity (rendered in stick model and colored according to atom type) as shown in Table S5. Target protein is illustrated with sub-domains color-coded according to chainbow. Complex **2** is depicted in sphere mode colored according to atom type by magenta C atoms, while co-crystallized NPS is rendered in stick representation and colored according to atom type by light pink C atoms. Hydrogen atoms of ligands are omitted for clarity. Both structures were ray-traced and illustrated with the aid of PyMol Molecular Graphics System.

global binding energies shown in Table 4 are in a good agreement. Complex **2** is revealed to have the highest K_b constant among the complexes, followed by **1**, **3** and **4** which has the lowest K_b constant, that is, the weakest binding (**2** > **1** > **3** > **4**). From the global binding energies, it is deduced that the highest energy (lowest binding capacity) is calculated for complex **4**, which also has the lowest K_b constant. Complexes **1**, **2** and **3** have the lowest binding energies, with small differences between them (**1** > **2** > **3** > **4**).

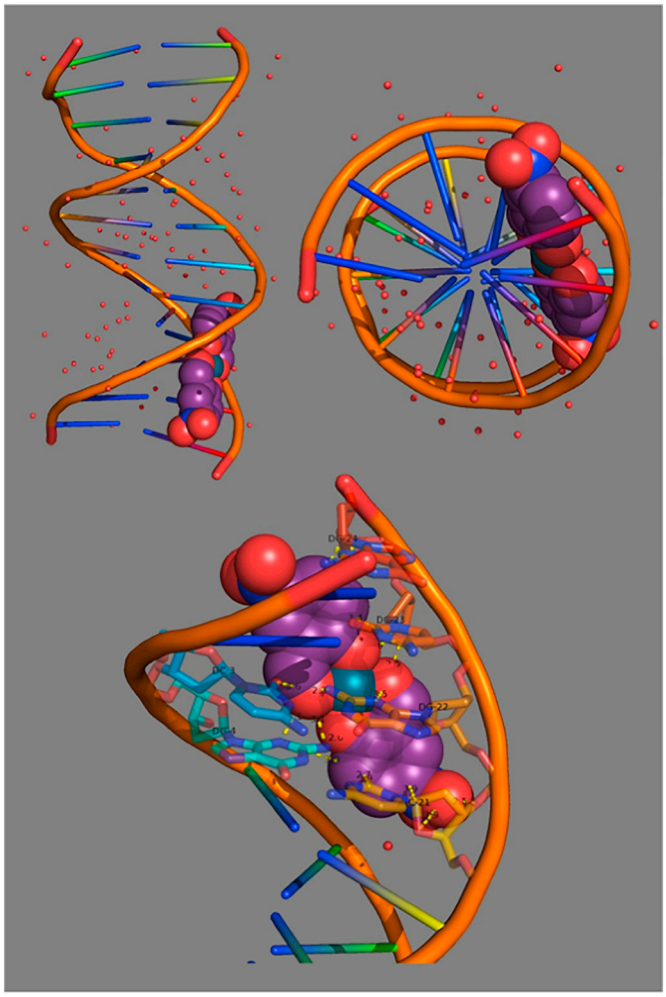

Fig. 10. Molecular docking of complex **2** in the crystal structure of CT DNA (PDB accession no. 1bna) in the binding cavity of minor groove of DNA. DNA structure is illustrated as cartoon color-coded according to chain in brown color, while docked molecule is represented in sphere model and colored according to atom type (in magenta C atoms). In upper right part is illustrated the docking pose from a view above the axis of the helix. In lower part is illustrated the ligand binding site architecture of complex **2** in the crystal structure of CT DNA. Binding interactions with nucleotide molecules are shown in Table S9. Nucleotides are rendered in semitransparent stick model and colored according to atom type. Yellow dotted lines indicate hydrogen bond, polar and hydrophobic interactions between the docked molecule and the nucleotides of the binding pocket in the minor groove of DNA. Hydrogen atoms are omitted from all molecules for clarity. The final structure was ray-traced. Nucleotides are numbered according to PyMol software. The final structure was ray-traced.

4. Conclusions

Four neutral mononuclear palladium complexes **1–4** of X-substituted salicylaldehyde (X = 3-OCH_3, 5-NO_2, 5-Cl, or 5-Br) were synthesized and characterized. The complexes are formulated as [Pd(3-OCH_3-salo)$_2$] **1**, [Pd(5-NO_2-salo)$_2$] **2**, [Pd(5-Cl-salo)$_2$] **3**, and [Pd(5-Br-salo)$_2$] **4**. The structure of complex **1** was determined by single-crystal X-ray crystallography, revealing square planar geometry of the palladium atom.

The ability of complexes **1–4** to bind to CT DNA and serum albumins was evaluated *in vitro* and *in silico*. The complexes may bind to CT DNA *via* intercalation and have relatively high DNA-binding constants (K_b). Complexes **1–4** exhibited similar or higher SA-fluorescence quenching ability and similar SA-binding affinity with free X-saloH and similar Pd complexes, as evaluated by the calculated k_q and K constants,

respectively. The values of the binding constants to SAs showed that complexes **1–4** are able to bind reversibly to the albumins in order to be transferred and get released upon arrival at the potential targets.

The results from the present molecular modeling simulations may provide useful complementary insights for the elucidation of the mechanism of action of the studied complexes at a molecular level. *In silico* procedures indicate better interaction of complex **2** with both HSA and BSA, compared to that of the rest complexes. The DNA-interaction of **1–3** complexes was found similar, from energetic point of view. Molecular modeling calculations can provide a molecular basis for the understanding of both the impairment of DNA by its binding with the studied complexes and also the ability of these compounds for transportation through BSA and possible interaction with other protein targets involved in various diseases. This study can provide information for the elucidation of the mechanism of action of both complexes in a molecular level.

The fact that the reported palladium complexes of substituted salicylaldehydes are able to interact with CT DNA and albumins is encouraging for the use as potential metallotherapeutic agents and giver further perspectives for the use of those complexes in biological fields.

Abbreviations

br	broad
BSA	bovine serum albumin
CT	calf-thymus
DFT	Density Functional Theory
DMF	*N*,*N*-dimethylformamide
DMSO	dimethylsulfoxide
EB	ethidium bromide, 3,8-diamino-5-ethyl-6-phenyl-phenanthridinium bromide
HSA	human serum albumin
IBP	ibuprofen, 2-(4-isobutylphenyl)propionic acid
K	SA-binding constant
K_{app}	apparent DNA-binding constant
K_b	DNA-binding constant
k_q	quenching constant
K_{SV}	Stern-Volmer constant
m	medium
NPS	naproxen, (*S*)-2-(6-methoxynaphthalen-2-yl)propanoic acid
PDB	Protein Data Bank
PMF	potential mean force
r	[compound]/[DNA] ratio
r′	[DNA]/[compound] ratio
RCSB	Research Collaboratory for Structural Bioinformatics
RMSD	root-mean squared deviation
RT	room temperature
s	strong
SA	serum albumin
saloH	salicylaldehyde
sh	shoulder
sm	strong-to-medium
vdw	van der Waals
w	weak
X-saloH	substituted salicylaldehyde

Appendix A. Supplementary data

CCDC 1854574 contains the supplementary crystallographic data for this paper. These data can be obtained free of charge *via* www.ccdc.cam.ac.uk/conts/retrieving.html (or from the Cambridge Crystallographic Data Centre, 12 Union Road, Cambridge CB21EZ, UK; fax: (+44) 1223-336-033; or deposit@ccde.cam.ac.uk). Supplementary data associated with this article can be found, in the online version, at doi:https://doi.org/10.1016/j.jinorgbio.2019.02.013

References

[1] M. Alam, F. Huq, Coord. Chem. Rev. 316 (2016) 36–67.
[2] M. Fanelli, M. Formica, V. Fusi, L. Giorgi, M. Micheloni, P. Paoli, Coord. Chem. Rev. 310 (2016) 41–79.
[3] S. Medici, M. Peana, V. Nurchi, J. Lachowicz, G. Crisponi, Coord. Chem. Rev. 284 (2015) 329–350.
[4] A. Garoufis, S.K. Hadjikakou, N. Hadjiliadis, Coord. Chem. Rev. 253 (2009) 1384–1397.
[5] F. Shaheen, A. Badshah, M. Gielen, G. Croce, U. Florke, S. Ali, J. Organomet. Chem. 695 (2010) 315–322.
[6] M. Gaber, H.A. El-Ghamry, S.K. Fathalla, Spectrochim. Acta Part A 139 (2015) 396–404.
[7] Y. Yang, P. Lu, T. Zhu, C. Liu, Acta Cryst E63 (2007) m1613.
[8] Q. Wang, D. Wang, Acta Cryst E64 (2008) m298.
[9] C. Pessoa, I. Cavaco, I. Correira, I. Tomaz, T. Duarte, P. Matias, J. Inorg. Biochem. 80 (2000) 35–39.
[10] M. Sumar Ristovic, A. Zianna, G. Psomas, A. Hatzidimitriou, E. Coutouli-Argyropoulou, M. Lalia-Kantouri, Mat. Sci. Eng. C 61 (2016) 579–590.
[11] E. Pelttari, E. Karhumaki, J. Langshaw, H. Perakyla, H. Elo, Z. Naturforsch. 62c (2007) 487–497.
[12] A. Jayamani, N. Sengottuvelan, G. Chakkaravarthi, Polyhedron 81 (2014) 764–776.
[13] M. Lalia-Kantouri, C.D. Papadopoulos, A.G. Hatzidimitriou, M.P. Sigalas, M. Quiros, S. Skoulika, Polyhedron 52 (2013) 1306–1316.
[14] M. Lalia-Kantouri, M. Gdaniec, T. Choli-Papadopoulou, A. Badounas, C.D. Papadopoulos, A. Czapik, G.D. Geromichalos, D. Sahpazidou, F. Tsitouroudi, J. Inorg. Biochem. 117 (2012) 25–34.
[15] A. Zianna, K. Chrissafis, A. Hatzidimitriou, M. Lalia-Kantouri, J. Therm. Anal. Calorim. 120 (2015) 59–66.
[16] A. Zianna, G. Psomas, A. Hatzidimitriou, E. Coutouli-Argyropoulou, M. Lalia-Kantouri, J. Inorg. Biochem. 127 (2013) 116–126.
[17] E. Mrkalić, A. Zianna, G. Psomas, M. Gdaniec, A. Czapik, E. Coutouli-Argyropoulou, M. Lalia-Kantouri, J. Inorg. Biochem. 134 (2014) 66–75.
[18] A. Zianna, G. Psomas, A. Hatzidimitriou, M. Lalia-Kantouri, RSC Adv. 5 (2015) 37495–37511.
[19] A. Zianna, M. Sumar Ristovic, G. Psomas, A. Hatzidimitriou, E. Coutouli-Argyropoulou, M. Lalia-Kantouri, J. Coord. Chem. 68 (2015) 4444–4463.
[20] A. Zianna, M. Sumar Ristovic, G. Psomas, A. Hatzidimitriou, E. Coutouli-Argyropoulou, M. Lalia-Kantouri, Polyhedron 107 (2016) 136–147.
[21] A. Zianna, G. Psomas, A. Hatzidimitriou, M. Lalia-Kantouri, Polyhedron 124 (2017) 104–116.
[22] A. Zianna, G. Psomas, A. Hatzidimitriou, M. Lalia-Kantouri, J. Inorg. Biochem. 163 (2016) 131–142.
[23] J. Marmur, J. Mol. Biol. 3 (1961) 208–211.
[24] M.F. Reichmann, S.A. Rice, C.A. Thomas, P. Doty, J. Am. Chem. Soc. 76 (1954) 3047–3053.
[25] Bruker Analytical X-ray Systems, Inc. Apex2, Version 2 User Manual, M86-E01078, WI, Madison, 2006.
[26] Siemens Industrial Automation, Inc. SADABS: Area-Detector Absorption Correction; Madison, WI, (1996).
[27] L. Palatinus, G. Chapuis, J. Appl. Crystallogr. 40 (2007) 786–790.
[28] P.W. Betteridge, J.R. Carruthers, R.I. Cooper, K. Prout, D.J. Watkin, J. Appl. Crystallogr. 36 (2003) 1487.
[29] D.J. Watkin, C.K. Prout, L.J. Pearce, CAMERON Program, Chemical crystallographic laboratory, Oxford University, UK (1996).
[30] A. Wolfe, G. Shimer, T. Meehan, Biochemistry 26 (1987) 6392–6396.
[31] G.A. Gamov, M.N. Zavalishin, V.A. Sharnin, Spectrochim. Acta Part A 206 (2019) 160–164.
[32] P. Thordarson, Chem. Soc. Rev. 40 (2011) 1305–1323.
[33] G. Scatchard, Ann. N. Y. Acad. Sci. 51 (1949) 660–672.
[34] G. Zhao, H. Lin, S. Zhu, H. Sun, Y. Chen, J. Inorg. Biochem. 70 (1998) 219–226.
[35] J. Jiang, X. Tang, W. Dou, H. Zhang, W. Liu, C. Wang, J. Zheng, J. Inorg. Biochem. 104 (2010) 583–591.
[36] J.R. Lakowicz, Principles of Fluorescence Spectroscopy, 3rd ed., Plenum Press, New York, 2006.
[37] L. Stella, A. L. Capodilupo, M. Bietti, Chem. Commun. (2008) 4744–4746.
[38] Y. Wang, H. Zhang, G. Zhang, W. Tao, S. Tang, J. Lumin. 126 (2007) 211–218.
[39] Spartan'08 v.1.1.4, Wavefunction Inc., Irvine, CA, USA; www.wavefun.com.
[40] A.D. Beke, Phys. Rev. A 38 (1998) 3098.
[41] C. Lee, W. Yang, R.G. Parr, Phys. Rev. B 37 (1988) 785–789.
[42] R.G. Parr, W. Yang, Density functional theory of atoms and molecules. New York: Oxford University Press; 1989. A standard valence double-zeta basis set, 6-31G*.
[43] W. Kohn, Rev. Mod. Phys. 71 (1999) 1253–1266.
[44] W. Koch, M.C. Holthausen, A Chemist's Guide to Density Functional Theory, 2nd ed., Wiley-VCH, Weinheim, 2001.
[45] C.E. Dykstra, G. Frenking, K.S. Kim, G.E. Scuseria (Eds.), Theory and Applications of Computational Chemistry: The First Forty Years, Elsevier B. V, Amsterdam, 2005.
[46] J. Ghuman, P.A. Zunszain, I. Petitpas, A.A. Bhattacharya, M. Otagiri, S. Curry, J. Mol. Biol. 353 (2005) 38–52.
[47] A. Bujacz, K. Zielinski, B. Sekula, Proteins 82 (2014) 2199–2208.
[48] H.M. Berman, J. Westbrook, Z. Feng, G. Gilliland, T.N. Bhat, H. Weissig, I.N. Shindyalov, P.E. Bourne, Nucleic Acids Res. 28 (2000) 235–242.
[49] H.M. Berman, K. Henrick, H. Nakamura, Nature Struct. Mol. Biol. 10 (2003) 980.
[50] F.C. Bernstein, T.F. Koetzle, G.J. Williams, E.E. Meyer, M.D. Brice, J.E. Rodgers, O. Kennard, T. Shimanouchi, M. Tasumi, J. Mol. Biol. 112 (1977) 535–542.

[51] H.R. Drew, R.M. Wing, T. Takano, C. Broka, S. Tanaka, K. Itakura, R.E. Dickerson, Proc. Natl. Acad. Sci. 78 (1981) 2179–83.]
[52] W.L. DeLano, The PyMOL molecular graphics system 0.99, DeLano scientific, San Carlos, CA, USA, 2006.
[53] W.J. Geary, Coord. Chem. Rev. 7 (1971) 81–122.
[54] R.M. Silverstein, G.C. Bassler, G. Morvill, Spectrometric Identification of Organic Compounds, 6th ed., Wiley, New York, 1998.
[55] K. Nakamoto, Infrared and Raman Spectra of Inorganic and Coordination Compounds, Part B: Applications in Coordination, Organometallic, and Bioinorganic Chemistry, 6th ed., Wiley, New Jersey, 2009.
[56] M. Ahmadi, A. Fasihizad, B. Machura, R. Kruszynski, A. Akbari, T. Barak, Can. J. Basic Appl. Sci. 3 (2015) 155–163.
[57] B.M. Zeglis, V.C. Pierre, J.K. Barton, Chem. Commun. (2007) 4565–4576.
[58] Q. Zhang, J. Liu, H. Chao, G. Xue, L. Ji, J. Inorg. Biochem. 83 (2001) 49–55.
[59] A.M. Pyle, J.P. Rehmann, R. Meshoyrer, C.V. Kumar, N.J. Turro, J.K. Barton, J. Am. Chem. Soc. 111 (1989) 3051–3058.
[60] E. Sindhuja, R. Ramesh, N. Dharmaraj, Y. Liu, Inorg. Chim. Acta 416 (2014) 1–12.
[61] P. Kalaivani, C. Umadevi, R. Prabhakaran, F. Dallemer, P.S. Mohan, K. Natarajan, Polyhedron 80 (2014) 97–105.
[62] S. Dhar, M. Nethaji, A.R. Chakravarty, J. Inorg. Biochem. 99 (2005) 805–812.
[63] B.C. Baguley, Mol. Cell. Biochem. 43 (1982) 167–181.
[64] B.F. Cain, B.C. Baguley, W.A. Denny, J. Med. Chem. 21 (1978) 658–668.
[65] M. Szumilak, A. Merecz, M. Strek, A. Stanczak, T.W. Inglot, B.T. Karwowski, Int. J. Mol. Sci. 17 (2016) 1560.
[66] D. Li, J. Tian, W. Gu, X. Liu, S. Yan, J. Inorg. Biochem. 104 (2010) 171–179.
[67] J.L. Garcia-Gimenez, M. Gonzalez-Alvarez, M. Liu-Gonzalez, B. Macias, J. Borras, G. Alzuet, J. Inorg. Biochem. 103 (2009) 923–934.
[68] C. Tolia, A.N. Papadopoulos, C.P. Raptopoulou, V. Psycharis, C. Garino, L. Salassa, G. Psomas, J. Inorg. Biochem. 123 (2013) 53–65.
[69] X. He, D.C. Carter, Nature 358 (1992) 209–215.
[70] R.E. Olson, D.D. Christ, Ann. Rep. Med. Chem. 31 (1996) 327–336.
[71] C. Tan, J. Liu, H. Li, W. Zheng, S. Shi, L. Chen, L. Ji, J. Inorg. Biochem. 102 (2008) 347–358.
[72] I. Petitpas, T. Grune, A.A. Bhattacharya, S. Twine, M. East, S. Curry, J. Mol. Biol. 314 (2001) 955–960.
[73] V. Rajendiran, R. Karthik, M. Palaniandavar, H. Stoeckli-Evans, V.S. Periasamy, M.A. Akbarsha, B.S. Srinag, H. Krishnamurthy, Inorg. Chem. 46 (2007) 8208–8221.
[74] S. Wu, W. Yuan, H. Wang, Q. Zhang, M. Liu, K. Yu, J. Inorg. Biochem. 102 (2008) 2026–2034.
[75] O.H. Laitinen, V.P. Hytonen, H.R. Nordlund, M.S. Kulomaa, Cell. Mol. Life Sci. 63 (2006) 2992–3017.
[76] S. Sugio, A. Kashima, S. Mochizuki, M. Noda, K. Kobayashi, Protein Eng. 12 (1999) 439.